Simultaneous fractionation of sulfur dioxide explains mass independent fractionation of sulfur isotopes in Archean sedimentary pyrites

M. Chen [a,b,*], Z. Huang [b], I.H. Campbell [b], M. Sambridge [b], J.N. Ávila [b,c]

[a] MOE Key Laboratory of Orogenic Belts and Crustal Evolution, School of Earth and Space Sciences, Peking University, Beijing 100871, China
[b] Research School of Earth Sciences, Australian National University, Canberra, ACT 0200, Australia
[c] Griffith Centre for Social and Cultural Research, Griffith University, Nathan, QLD 4111, Australia

ARTICLE INFO

ABSTRACT

The relationship between $\Delta^{36}S$ and $\Delta^{33}S$ in Archean sedimentary pyrites has been used to evaluate early geologic processes, including photochemical reactions in the anoxic atmosphere, biological activity and thermochemical alteration during sediment deposition. We have applied statistical methods to quadruple S isotope analyses of Archean sedimentary pyrites, using data compiled from the literature. Most of the best-fit lines, on plots of $\Delta^{36}S$ against $\Delta^{33}S$, have Archean reference array-like $\Delta^{36}S/\Delta^{33}S$ slopes that vary between -1.5 and -0.9. Rigorous statistical tests were conducted to calculate the probability of the best-fit lines passing through the origin. Seventeen of 23 $\Delta^{36}S$-$\Delta^{33}S$ regression lines, which pass our reliability filter of $R^2 \geq 75\%$ and $\Delta^{33}S$ range $\geq 2\permil$, have positive intercepts on the $\Delta^{36}S$ axis, and 13 of these have a probability of $< 5\%$ of a zero intercept on the $\Delta^{36}S$ axis. The observed $\Delta^{36}S/\Delta^{33}S$ slopes and the non-negative intercepts, which requires at least two mass-independent fractionation source reactions to operate simultaneously, can be produced by UV radiation in the atmosphere at low SO_2 partial pressures by combining collision-induced intersystem crossing in the SO_2 photoexcitation band (240–340 nm), with the self-shielding effect in the SO_2 photolysis band (190–220 nm). The two SO_2 photochemical processes must occur simultaneously in a single atmospheric reservoir in order that the fraction contributed by the end-member process remains constant across the full range of $\Delta^{33}S$ values. We call this process *simultaneous fractionation*. We applied a two-end-member model to calculate the fraction of S contributed by the SO_2 photoexcitation end-member (f) needed to produce the observed $\Delta^{36}S/\Delta^{33}S$ gradients and variable intercepts on the $\Delta^{36}S$ axis in the Archean sedimentary pyrites, when the other end-member is SO_2 photolysis with the self-shielding. The simplest explanation for variations in f, and therefore variations in $\Delta^{36}S/\Delta^{36}S$ gradients, is that it is controlled by changes in the partial pressure of SO_2 in the atmosphere.

1. Introduction

Mass independent fractionation (MIF) of ^{33}S, measured as $\Delta^{33}S$, is the departure in ^{33}S from the expected relationship between $\delta^{33}S$ and $\delta^{34}S$ predicted from mass dependent fractionation (Farquhar et al., 2000) and it occurs in an oxygen free atmosphere when volcanic SO_2 dissociates into S^0 and SO_4^{2-} in the presence of ultraviolet light (Farquhar et al., 2001). Ono et al. (2003) suggested that the Archean atmospheric photochemical reactions produced S^0 with positive $\Delta^{33}S$ and $\delta^{34}S$, and H_2SO_4, that is negative in both isotopes. MIF of ^{33}S is accompanied by MIF of ^{36}S, measured as $\Delta^{36}S$, so that when $\Delta^{36}S$ is plotted against $\Delta^{33}S$ the data lie on a fractionation line. The slope of this line depends on the wavelength of the ultraviolet light and composition

of the atmosphere in which SO_2 photochemistry takes place (Masterson et al., 2011; Ono et al., 2013; Whitehill et al., 2015; Whitehill and Ono, 2012; Whitehill et al., 2013). If, as is generally assumed, the isotopic composition of sulfur in Earth's mantle is chondritic, mantle $\Delta^{36}S$, $\Delta^{33}S$, and $\delta^{34}S$ are near zero (Labidi et al., 2014). If $\Delta^{36}S$ is fractionated from $\Delta^{33}S$ by a single MIF process the fractionation line must therefore pass through the origin.

Archean sedimentary pyrites typically show a correlated variation between $\Delta^{36}S$ and $\Delta^{33}S$ values with $\Delta^{36}S/\Delta^{33}S$ ratios between -1.5 and -0.9 (Farquhar et al., 2000; Kaufman et al., 2007; Zerkle et al., 2012). The array formed by the correlation between $\Delta^{36}S$ and $\Delta^{33}S$, together with the $\Delta^{33}S$-$\delta^{34}S$ relationship with a slope of ~0.9, have been termed the Archean Reference Array (ARA) (Ono, 2017; Ono et al., 2009).

Measurements of four stable sulfur isotopes in pyrites from early Archean bedded barite deposits revealed significant deviations from the ARA-like $\Delta^{36}S/\Delta^{33}S$ array with correlation slopes lower than the ARA and negative intercept values on the $\Delta^{36}S$ axis (Muller et al., 2017; Roerdink et al., 2016; Shen et al., 2009). The origin of non-zero intercepts is uncertain. Shen et al. (2009) proposed microbial sulfate reduction (MSR) for the sedimentary barite from the ~3.47 Ga Dresser Formation, NW Australia, whereas a complex three-step mixing model has been suggested for hydrothermal barite deposits for both the 3.55–3.51 Ga Theespruit Formation, Lower Onverwacht Group in the Barberton Greenstone Belt, Swaziland (Roerdink et al., 2016) and the 3.2 Ga Sargur Group, India (Muller et al., 2017). Roerdink et al. (2016) interpreted the observed deviation from the ARA-like $\Delta^{36}S/\Delta^{33}S$ array and the negative $\Delta^{36}S$ intercept as the result of a three-stage process: 1) production of a precursor sulfide with a non-ARA $\Delta^{36}S/\Delta^{33}S$ slope via dissociation of SO_2 by the self-shielding mechanism of Ono et al. (2013), 2) reworking of atmospheric sulfide into the hydrothermal system, and 3) mixing with the MSR-reduced seawater sulfate (Roerdink et al., 2016) or thermally reduced barite sulfate at higher temperature (Muller et al., 2017). In contrast, Archean sedimentary pyrites with ARA-like $\Delta^{36}S$-$\Delta^{33}S$ linear trends show positive $\Delta^{36}S$ intercepts (Farquhar et al., 2013; Galić et al., 2017; Izon et al., 2017; Ono et al., 2009; Williford et al., 2016). Ono et al. (2009) fitted a least-square linear regression to the results of 13 analyses of pyrites from a sedimentary layer in the ~2.5 Ga Klein Naute Formation and obtained an equation of $\Delta^{36}S = -0.86*\Delta^{33}S + 0.27$. The $\Delta^{36}S/\Delta^{33}S$ slope of -0.86 was recognized as being ARA-like but the implications of the positive $\Delta^{36}S$ intercept was not addressed. Williford et al. (2016) also noticed a positive $\Delta^{36}S$ intercept of $+1.4‰$ for the best-fit line for $\Delta^{36}S$-$\Delta^{33}S$ data for pyrites from the lower units of the ~2.5 Ga Mt. McRae Shale and attributed it to the microbial sulfate reduction. MSR, however, shifts the $\Delta^{36}S$ to more negative values (Farquhar et al., 2003; Johnston et al., 2007; Ono et al., 2006b), making this interpretation highly unlikely. The origin of the positive $\Delta^{36}S$ intercepts, recorded by Archean sedimentary pyrites, with $\Delta^{36}S/\Delta^{33}S$ slopes similar to the ARA, has not been addressed. A notable exception is a study by Gallagher et al. (2017) who attributed a positive intercept in sedimentary pyrites from the ~2.5 Ga Gamohaan Formation, South Africa, to recycling of crustal S-MIF from local arc-volcanic eruptions.

In this study we apply statistical methods to the compiled pyrite quadruple S isotope data from global Archean sediments, and show that some of the fitted lines for the pyrite $\Delta^{36}S$-$\Delta^{33}S$ correlation arrays have statistically significant positive intercepts on the $\Delta^{36}S$ axis. We argue that the observed linear $\Delta^{36}S$-$\Delta^{33}S$ arrays cannot be the result of mixing of sulfur from two or more independent reservoirs but can be the product of the simultaneous fractionation of SO_2 in an anoxic atmosphere by a combination of photochemical reactions in the 250–330 nm and 190–220 nm bandwidths.

2. $\Delta^{36}S/\Delta^{33}S$ relationships of the Archean sedimentary pyrites

Linear regression lines were fitted to 42 suites of Archean sedimentary pyrites (Table A.1) for which quadruple sulfur isotope analyses are available. Least squares linear regressions for their $\Delta^{36}S$-$\Delta^{33}S$ distributions, were solved using a Python code written specifically for this study (see *Supplementary materials*), and the results are listed in Table 1. The solutions were calculated by building a G matrix, and tested with Chi-square of goodness of fit, as well as Critical Chi-square for 5, 50, and 95%. The confidence and *P*-value for the probability of fit were also calculated. The external uncertainties for the compiled pyrite data, which were calculated by combining the single analysis uncertainties for each individual analysis measured with the standard deviation of the reference materials, were applied to the linear regression. The uncertainties in the parameters of the best-fit line were further amplified by taking the scatter of the data into account. This procedure leads to a conservative estimate of the *p*-value for the fitted line passing through the origin, and is therefore the most rigorous statistical test for a non-

zero intercept.

Fig. 1 shows the linear regression lines for two Archean sedimentary pyrite suites, NF-LOW1 and NF-UP4A, from the ~2.6 Ga Nauga Formation (Farquhar et al., 2013; Izon et al., 2017). The NF-UP4A pyrite suite was measured by the SF_6 IR-MS method, whereas the NF-LOW1 suite was measured by in-situ SIMS technique. They both show excellent inverse correlations between $\Delta^{36}S$ and $\Delta^{33}S$ (Farquhar et al., 2013; Izon et al., 2017). The data for the two pyrite suites are distributed around linear correlation lines, as expected, and their slopes of -1.21 ± 0.01 and -1.04 ± 0.03 (1SD) fall within the ARA range (Fig. 1a and b, Table 1). What is unexpected is that the correlation lines fitted to the NF-UP4A and NF-LOW1 data do not pass within uncertainty of the origin, with intercepts of $+0.49 \pm 0.11‰$ and $+0.81 \pm 0.03‰$ (1SD) on the $\Delta^{36}S$ axis (Fig. 1c and d, Table 1). The calculated *p* values for the probability of the correlation lines passing through the origin are less than 0.000,002 and 0.000,001 respectively (Table 1, Fig. A.1). The Python code, used to calculate the *p*-values, takes into account both the scatter in unknown data, and the combined precision errors of unknowns and reference materials, which increases the calculated uncertainty on the intercept. Furthermore, the quadruple S isotopic compositions of the two sedimentary pyrite suites were obtained by two different analyzation techniques. Failure of the two $\Delta^{36}S$-$\Delta^{33}S$ correlation lines to pass within uncertainty of the origin, therefore cannot be attributed to underestimation of analytical errors or to an instrumental effect.

A literature survey has shown that failure of the NF-UP4A and NF-LOW1 $\Delta^{36}S$-$\Delta^{33}S$ correlation lines to pass through the origin is not unique. We compiled $\Delta^{36}S$-$\Delta^{33}S$ data from 38 Archean sedimentary suites with linear correlations ($R^2 \geq 50\%$). The reliability of slope and intercept of the $\Delta^{36}S$-$\Delta^{33}S$ linear regression lines increases with the R^2 value and $\Delta^{33}S$ range. Therefore, we have considered only suites with $R^2 \geq 75\%$ and a $\Delta^{33}S$ range $\geq 2‰$ (Fig. 2). Twenty-three of the 38 Archean sedimentary suites passed these criteria. Seventeen of the 23 correlation lines have positive intercepts on the $\Delta^{36}S$ axis of up to $+1.4‰$ and 13 of these have a probability of less than 5% of the intercept on the $\Delta^{36}S$ axis being zero. Of the remaining 6 data sets, with negative intercepts on the $\Delta^{36}S$ axis, 2 have a moderate probability ($> 20\%$) of passing through the origin. The other 4 have a probability of less than 1% of a zero intercept on the $\Delta^{36}S$ axis, the lowest being $-1.07‰ \pm 0.22‰$ (1SD). The probability of the intercepts on the $\Delta^{33}S$ axis being zero was also calculated and the results are similar to those reported for $\Delta^{36}S$ axis (Table A.2). Detailed descriptions of the linear fits for the compiled Archean sedimentary pyrites are given in *Supplementary materials*.

3. Non-zero intercepts for the Archean $\Delta^{36}S$-$\Delta^{33}S$ correlations

The best-fit lines for the sedimentary pyrite suites NF-UP4A and NF-LOW1, together with the majority sedimentary pyrite suites from the other Archean locations (Farquhar et al., 2013; Farquhar et al., 2007; Izon et al., 2017; Kaufman et al., 2007; Ono et al., 2009; Thomazo et al., 2009; Thomazo et al., 2013; Williford et al., 2016; Zhelezinskaia et al., 2014), have statistically positive intercepts on both the $\Delta^{36}S$ and $\Delta^{33}S$ axes (Table A. 2; Fig. 2). The probability of the best-fit lines for the pyrite suites NF-UP4A and NF-LOW1 not having positive intercepts on the $\Delta^{36}S$ axis is low to negligible respectively, and this is also true for many of the other suites listed in Table 1 and plotted in Fig. A.1.

As noted in the Introduction, if primitive S, which is assumed to have $\Delta^{33}S = \Delta^{36}S = 0$, is fractionated by a single event, $\Delta^{36}S$ and $\Delta^{33}S$ will lie on a linear array that passes through the origin. The observation that the best-fit correlation lines for NF-UP4A and NF-LOW1, and samples from most other Archean locations, do not pass through the origin, requires that at least two processes are involved in the fractionation of $\Delta^{36}S$ from $\Delta^{33}S$. There are five fractionation processes that are known to produce variations in $\Delta^{33}S$ and $\Delta^{36}S$ (Fig. 3):

Table 1
Linear regression fitting results for the Archean sedimentary pyrites.

Age (Ma)	Stratigraphic units	Region	Sample ID	Method	No.	$\Delta^{33}S$ range (‰)	$\Delta^{36}S/\Delta^{33}S$	σ	$\Delta^{36}S$ intercept	σ	R^2 value	P-value*	Ref.
>3800	Ujaraaluk metasediments	Québec	NGB	SF6	13	2.09	−0.85	0.18	−0.62	0.28	0.67	0.01	Thomassot et al., 2015
3481	Dresser Formation	Western Australia											
			DF1	SF6	15	1.29	−1.37	0.37	−0.59	0.25	0.52	0.008053	Shen et al., 2009
			DF2	SF6	22	4.61	−0.81	0.04	−0.21	0.05	0.93	0.000029	Ueno et al., 2008
			DF3	SIMS	23	1.92					no trend		Wacey et al., 2015
3334	Mendon Formation	South Africa	MNF	SF6	5	2.47	−0.47	0.19	−0.65	0.29	0.67	0.010874	Busigny et al., 2017
3259	Mapepe Formation	South Africa											
			MF-BARITE	SIMS	81	1.04	−3.56	0.27	−0.70	0.07	0.69	0	Roerdink et al., 2013
			MF-CHERT	SIMS	42	3.48	−0.87	0.11	0.08	0.11	0.51	0.237525	Roerdink et al., 2013
			MF-SHALE	SF6	8	1.86	−0.64	0.13	−0.43	0.26	0.81	0.049095	Montinaro et al., 2015
3220	Moodies Group	South Africa	MDG	SF6	17	0.20					no trend		Saitoh et al., 2020
3137	Bababudan Group	South India	BG	SF6	12	1.95	−1.47	0.21	−0.03	0.13	0.83	0.408052	Mishima et al., 2017
2919	Vanivilas Formation	South India	VF	SF6	7	1.77	−1.17	0.14	−0.13	0.09	0.94	0.081079	Mishima et al., 2017
2839	Mozaan group	South Africa	MG	SF6	8	0.88					no trend		Ono et al., 2006a, 2006b
2740	Temagami greenstone belt	Canada	TGB	SF6	47	3.15	−0.74	0.07	0.042	0.06	0.74	0.226627	Diekrupa et al., 2018
			TGB-BIF	SF6	21	1.25	−1.38	0.21	0.351	0.14	0.70	0.005488	Diekrupa et al., 2018
			TGB-CHERT	SF6	8	0.55	−0.63	0.24	0.022	0.14	0.53	0.438438	Diekrupa et al., 2018
			TGB-VOLC	SF6	13	2.37	−0.57	0.08	0.029	0.08	0.81	0.351387	Diekrupa et al., 2018
			TGB-SHALE	SF6	5	1.64	−0.90	0.08	0.342	0.13	0.98	0.003321	Diekrupa et al., 2018
2720	Tumbiana Formation	Western Australia	TF	SF6	34	1.89	−1.61	0.14	0.23	0.09	0.80	0.003172	Thomazo et al., 2009; Farquhar et al., 2007
2713	Kidd Creek rhyolitic complex	Canada	KCRC	SF6	62	4.90	−0.93	0.06	0.12	0.08	0.81	0.083647	Kurzweil et al., 2013
2676	Ingaldhal Formation	South India	IF	SF6	14	5.00	−0.77	0.11	−1.07	0.22	0.80	0.000001	Mishima et al., 2017
2660	Batatal Formation	Brazil	BF	SF6 & SIMS	147	5.95	−0.93	0.04	0.20	0.06	0.79	0	Zhelezinskaia et al., 2014
2639	Jeerinah Formation	Western Australia	JF	SIMS	19	13.19	−0.89	0.04	0.89	0.45	0.97	0.023239	Williford et al., 2016
2635	Lokammo Formation	South Africa	LF	SF6	9	4.90	−1.02	0.04	0.28	0.21	0.99	0.085229	Zerkle et al., 2012
2633	Hiriyur Formation	South India	HF	SF6	13	5.05	−0.95	0.06	−0.31	0.07	0.96	0.000001	Mishima et al., 2017
2633	Carawine dolomite	Western Australia	CD	SIMS	15	0.78					no trend		Williford et al., 2016
2601	Cheshire Formation	Zimbabwe	CF	SF6	22	0.96	−1.66	0.24	0.26	0.15	0.71	0.043238	Thomazo et al., 2013
2588	Lower Nauga Formation	South Africa											
			NF-LOW1	SIMS	156	10.88	−1.21	0.01	0.81	0.03	0.99	0	Farquhar et al., 2013
			NF-LOW2	SF6	19	5.30	−0.98	0.09	−0.01	0.45	0.87	0.492908	Zerkle et al., 2012
2549	Upper Nauga Formation	South Africa											
			NF-UP1	SIMS	47	9.05	−0.97	0.05	−0.30	0.31	0.81	0.166639	Farquhar et al., 2013
			NF-UP2	SF6	15	4.10	−1.07	0.26	−0.65	1.30	0.57	0.307455	Zerkle et al., 2012
			NF-UP3	SF6	8	9.19	−0.90	0.01	−0.09	0.03	1.00	0.00031	Ono et al., 2009
2552	Upper Nauga Formation	South Africa											
			NF-UP4H	SF6	29	5.60	−1.58	0.12	1.14	0.54	0.86	0.016571	Izon et al., 2017
			NF-UP4A	SF6	55	6.51	−1.04	0.03	0.49	0.11	0.96	0.000002	Izon et al., 2017
2521			GF1	SF6	14	10.89	−0.86	0.09	0.05	0.40	0.89	0.452003	

Table 1 (*continued*)

Age (Ma)	Stratigraphic units	Region	Sample ID	Method	No.	Δ33S range (‰)	Δ36S/Δ33S	σ	Δ36S intercept	σ	R2 value	P-value*	Ref.
	Gamohaan Formation	South Africa											Kaufman et al., 2007
2521	Gamohaan Formation	South Africa	GF2	SIMS	88	9.55	−1.00	0.02	−0.41	0.13	0.96	0.000557	Gallagher et al., 2017
			GF2-STEEP	SIMS	17	3.99	−1.19	0.12	0.32	0.31	0.88	0.151732	Gallagher et al., 2017
			GF2-SHALLOW	SIMS	71	5.62	−0.91	0.02	−0.99	0.14	0.95	0	Gallagher et al., 2017
2521	Klein Naute Formation	South Africa	KNF	SF6	21	5.33	−1.01	0.08	0.25	0.14	0.90	0.033467	Ono et al., 2009
2501	Mt. McRae Shale	Western Australia	MMS1	SF6	42	11.52	−0.85	0.03	0.17	0.09	0.96	0.02213	Kaufman et al., 2007
			MMS1-UP	SF6	25	5.63	−1.02	0.06	0.30	0.11	0.93	0.004403	Kaufman et al., 2007
			MMS1-LOW	SF6	17	11.52	−0.82	0.02	0.15	0.07	0.99	0.018713	Kaufman et al., 2007
2500	Mt. McRae Shale	Western Australia	MMS2	SIMS	24	14.83	−0.85	0.03	0.90	0.18	0.96	0	Williford et al., 2016
			MMS2-UP	SIMS	15	8.14	−1.03	0.06	0.72	0.15	0.95	0.000001	Williford et al., 2016
			MMS2-LOW	SIMS	9	12.25	−0.88	0.03	1.39	0.24	0.99	0	Williford et al., 2016
2465	Kuruman Iron Formation	South Africa	KIF	SF6	9	2.91	−1.58	0.20	0.62	0.45	0.90	0.084866	Kaufman et al., 2007
2415	Koegas Subgroup	South Africa	KF	SF6	24	2.01	−1.26	0.19	0.16	0.14	0.68	0.132752	Johnson et al., 2013

*P value for null hypothesis that the $\Delta^{36}S$ intercept is equal to zero. When *P* value shows as zero, means P value <0.000001.

* Uncertainties are expressed as 1 sigma (1SD).

1. Isotopologue-dependent SO_2 photoexcitation via collision-induced intersystem crossing at wavelengths of 240–340 nm. At low SO_2 partial pressures, appropriate to the Archean atmosphere, this results in a $\Delta^{36}S$-$\Delta^{33}S$ fractionation line with a slope of +0.7 on a plot of $\Delta^{36}S$ against $\Delta^{33}S$ (Endo et al., 2016; Whitehill and Ono, 2012). At high SO_2 partial pressures, the experimental $\Delta^{36}S/\Delta^{33}S$ slopes can be up to +2.2 (Whitehill et al., 2013).
2. Isotopologue self-shielding in SO_2 photolysis at 190–220 nm wavelength, which produces negative $\Delta^{36}S$-$\Delta^{33}S$ relationships, normally a mixture of mutual-shielding and ideal self-shielding with slopes that vary between −6.8 and − 1.9, depending on the SO_2 partial pressures (e.g., Endo et al., 2016; Masterson et al., 2011; Ono, 2017; Ono et al., 2013; Whitehill and Ono, 2012). At low SO_2 partial pressures (pSO_2 < 10 Pa), appropriate for the Archean atmosphere, this photodissociation gives a slope of −2.4 (Endo et al., 2016).
3. Isotopologue-dependent absorption cross-section at 190–220 nm wavelength, which produces a small S-MIF signal with $\Delta^{33}S$ varying by less than +9‰ but with no clear correlation between $\Delta^{33}S$ and $\Delta^{36}S$ (Endo et al., 2015).
4. Microbial sulfate reduction (MSR) produces the Phanerozoic MDF line with a $\Delta^{36}S/\Delta^{33}S$ slope of −6.9 and a $\Delta^{36}S$ range of −1.9‰ to −2.4‰ (Ono et al., 2006b).
5. The magnetic isotopic effect in thermochemical sulfate reduction (TSR), which fractionates $\Delta^{33}S$ without affecting $\Delta^{36}S$ ($0 < \Delta^{33}S \leq +13‰$, $\Delta^{36}S \approx 0$) (Oduro et al., 2011).

All of the above $\Delta^{36}S$-$\Delta^{33}S$ correlation lines pass through the origin (Fig. 3) but none has a slope similar to the best-fit lines depicted in Figs. 1 and 2 for Archean samples. The challenge is to find a process, or combination of processes, that can produce the slopes and non-zero $\Delta^{36}S/\Delta^{33}S$ axis intercepts shown in Figs. 1 and 2 and documented in Table 1.

The carbon-rich nature of the host sediments to many of the Archean pyrites, NF-UP4A for example, are suggestive of biological activity. As a consequence, some biological fractionation of S isotopes is likely. However, MSR cannot explain the linear form of the best-fit lines for the NF-UP4A pyrites, nor their positive intercepts on the $\Delta^{36}S$ axis, for two reasons. First, all the analysed S from NF-UP4A have positive $\Delta^{33}S$ values (Fig. 1), which shows that the $\Delta^{33}S$ signal was derived dominantly from S^0 and not SO_4^{2-}. Second, MSR lowers $\Delta^{36}S$ but increases $\Delta^{33}S$ (Ono et al., 2006b), the effect on $\Delta^{36}S$, however, is much greater than on $\Delta^{33}S$ (Fig. 3). As a consequence, MSR reduces, not increases, the intercept on the $\Delta^{36}S$ axis (Fig. 3). It can explain the negative intercepts on the $\Delta^{36}S$ axis for the barite-associated pyrites from the North Pole, Pilbara Craton, Western Australia (Ueno et al., 2008; Shen et al., 2009) and the Barberton Greenstone Belt, South Africa (Roerdink et al., 2013), where there is convincing evidence that MSR has been active but it cannot explain the positive $\Delta^{36}S$ intercepts seen in most Archean pyrite suites (Fig. 2).

Thermochemical sulfate reduction (TSR), like MSR requires sulfate reduction, which as already noted, is inconsistent with the positive $\Delta^{33}S$ values found in NF-UP4A and most other Archean sedimentary pyrite suites. Furthermore, TSR requires temperatures close to 300 °C (Oduro et al., 2011). The Upper Nauga Formation is a plus 200-m-thick C-rich marine sediment (Izon et al., 2017), so TSR could not be important during in situ pyrite precipitation at realistic ocean temperatures. It could, however, take place during sulfide formation in submarine black smokers by reduction of seawater sulfate entrained into the rising hydrothermal plume. Because the high rate of entrainment in turbulent plumes (Turner, 1973), leads to extreme thermal gradients, TSR would have to occur within approximately 10 cm of the chimney vent. Although possible under such circumstances TSR is unlikely to be important. Finally, TSR cannot explain the negative intercepts on the $\Delta^{36}S$ axis seen in some Archean pyrite suites, for example, the North Pole.

We now discuss an alternative explanation for the non-zero intercepts on the $\Delta^{36}S$ and $\Delta^{33}S$ axes observed in the NF-UP4A pyrites, and many other Archean examples.
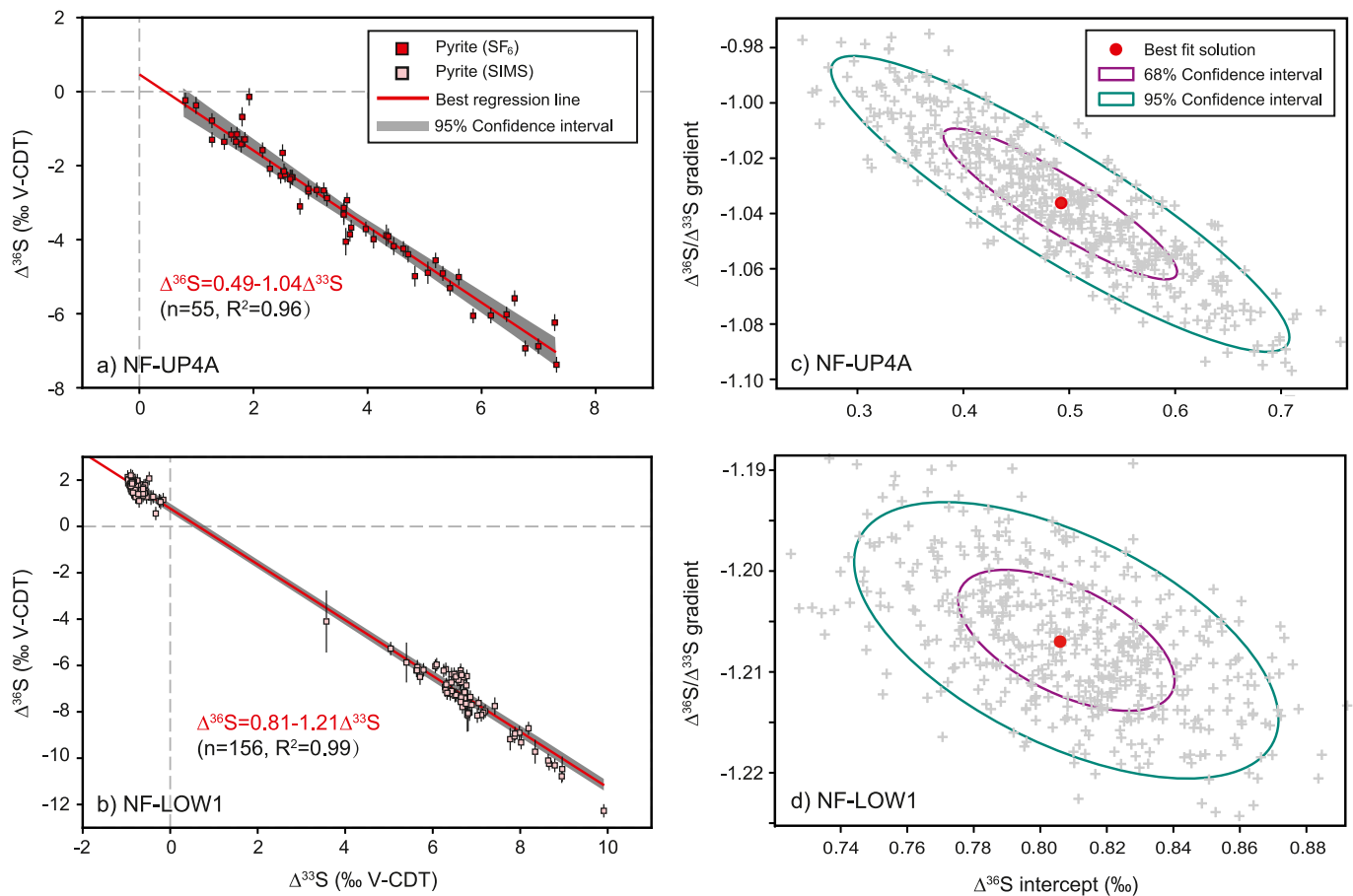
Fig. 1. a-b) Plots of $\Delta^{36}S$ vs. $\Delta^{33}S$ for two Archean sedimentary pyrite suites. Red squares represent the NF-UP4A pyrite suite, and pink squares the NF-LOW1 pyrite suite. One-sigma external uncertainties for $\Delta^{36}S$, shown in panels a-b as vertical black lines. One-sigma external uncertainties for $\Delta^{33}S$, which are much smaller than the data symbols, are not shown. The red solid lines are the best-fit linear regression lines for each data set, grey-shaded areas are the 95% confidence limits for the best-fit lines (Python code for least-squared linear regression fitting is given in *Supplementary materials*); c-d) Random draws of feasible solutions for the fitted $\Delta^{36}S$/ $\Delta^{33}S$ gradient and $\Delta^{36}S$ intercept (‰) for NF-UP4A and NF-LOW1. Each cross represents a random draw from the model error distribution for the gradient-intercept pair. Red dots represent the mean of the distribution of gradient and intercept pairs, i.e., the red solid lines in panels a-b; blue and green ellipses are 68% and 95% confidence levels, respectively. The grey crosses within the green ellipses are the grey area in panels a-b.

4. Quadruple-sulfur isotope fractionation by simultaneous fractionation of SO_2

Atmospheric mixing, i.e., SO_2 fractionation by two atmospheric processes known from experimental studies, has been suggested as a potential mechanism by several researchers (e.g., Whitehill and Ono, 2012; Endo et al., 2016; Mishima et al., 2017). Whitehill and Ono (2012) suggested "mixing the signatures of the 190-220 nm band and the 250-330 nm band in the right proportions could produce the Archean $\Delta^{36}S$/ $\Delta^{33}S$ ratio of -0.9" but did not expand on this statement or attempt to show how the known experimental arrays can be combined to produce the observed Archean linear arrays. Endo et al. (2016) also argued for a mixed signature from the 190–220 nm and the 250–330 nm bands and suggested that a minimum of 3.3% S input from photoexcitation is required to produce the $\Delta^{36}S$/$\Delta^{33}S$ ratio of the ~2.5 Ga Mt. McRae Formation. Similarly, Mishima et al. (2017) suggested an atmospheric mixing model in which "the SO_2 self-shielding rate and photoexcitation rate grew after 2.7 Ga" to explain variations in $\Delta^{36}S$/$\Delta^{33}S$ ratios. These atmospheric mixing models, without exception, overlooked the pervasive existence of non-zero $\Delta^{36}S$ and $\Delta^{33}S$ intercepts in the Archean sedimentary records. Crucially, the observed Archean linear arrays cannot be the result of mixing of sulfur from two or more independent atmospheric reservoirs, as the resulting mixture would not form a straight line but scatter over a broad field, as will be discussed in greater

detail below.

Therefore, we propose an alternative explanation, which is consistent with the Archean sedimentary data, that the observed best-fit lines are the product of simultaneous isotopic fractionation of SO_2 by two or more of the atmospheric processes known from experimental studies. These SO_2 photochemical processes must occur simultaneously, in a single atmospheric reservoir, in order that the fraction contributed by the end-member process remains constant across the full range of $\Delta^{33}S$ values. The difference between mixing and simultaneous fractionation may appear to be semantic so we give simple illustration to explain the difference. If the fractionation of S isotopes in NF-UP4A were produced by S in one reservoir (Reservoir A), lying on the photoexcitation line, mixing with S from a second reservoir (Reservoir B) that was fractionated by the self-shielding photolysis process, the S isotopes in both reservoirs, prior to mixing, would be distributed along two straight lines as shown in Fig. 3. The S isotope distribution in both reservoirs would, of course, be heterogeneous. For illustrative purposes, we have assumed that the end-members of these linear reservoirs can be represented by A_1 and A_2, and B_1 and B_2 respectively. If mixed occurred within reservoir A the compositions produced could lie anywhere on the A_1-A_2 straight line, but the end members would converge and eventually meet if mixing progressed to the point where the mixture became homogeneous. The same logic applies to mixing with Reservoir B. Mixing between linear arrays A and B, however, would produce a scatter of data
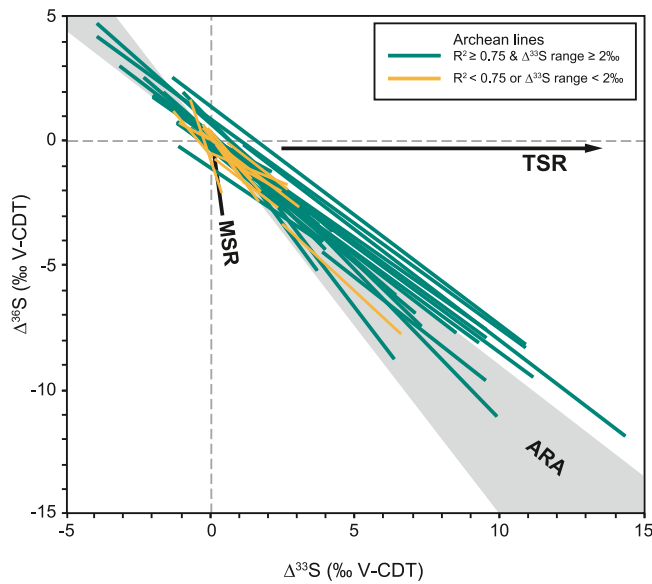
Fig. 2. The best-fit lines for $\Delta^{36}S$-$\Delta^{33}S$ correlations of the Archean sedimentary pyrite suites. The range of $\Delta^{36}S/\Delta^{33}S$ gradients for the Archean Reference Array (ARA) (Ono, 2017), the Phanerozoic microbial sulfate reduction (MSR) mass-dependent fractionation line (Ono et al., 2006b), and thermochemical sulfate reduction line (TSR) (Oduro et al., 2011), are also plotted. Over half of the best-fit lines for Archean suites, with high-reliability (green lines, $R^2 \geq 0.75$ and $\Delta^{33}S$ ranges $\geq 2‰$), have positive $\Delta^{36}S$ intercepts. Archean suites with low reliability (yellow lines, $R^2 < 0.75$ or $\Delta^{33}S$ ranges $< 2‰$) are also shown for comparison. The data for linear regression lines are from Busigny et al. (2017); Thomassot et al. (2015); Montinaro et al. (2015); Diekrupa et al. (2018); Gallagher et al. (2017); Mishima et al. (2017); Shen et al. (2009); Ueno et al. (2008); Roerdink et al. (2013); Thomazo et al. (2009); Farquhar et al. (2007); Kurzweil et al. (2013); Zhelezinskaia et al. (2014); Zerkle et al. (2012); Williford et al. (2016); Thomazo et al. (2013); Farquhar et al. (2013); Ono et al. (2009); Kaufman et al. (2007) and Johnson et al. (2013). Four Archean sedimentary suites showing no statistically reliable linear trend ($R^2 < 0.50$), including those from Ono et al. (2006a), Wacey et al. (2015), Williford et al. (2016) and Saitoh et al. (2020), are not shown. (For interpretation of the references to colour in this figure legend, the reader is referred to the web version of this article.)

lying between the four end member reservoirs, that is a quadrilateral, as illustrated in Fig. 3. Mixing between endmember A_1 and B_1 can produce points that lie anywhere on the line between A_1 and B_1, mixing between endmembers A_1 and B_2, will produce points that lie on the line between A_1 and B_2, etc. A linear array can only be preserved if mixing occurs within a single linear array. The two fractionation processes must occur simultaneously in a single reservoir –*simultaneous fractionation*– as is expected when atmospheric SO_2 is exposed to natural light with a continuum of wavelengths.

The model we have used to constrain how the experimental arrays can combine to produce the observed Archean linear arrays is illustrated in Fig. 4. We accept the arguments of Endo et al. (2016) that the 190–220 nm wavelength experiments, carried out prior to theirs, were run at inappropriately high pSO_2 (>1000 Pa), equivalent to >10,000 ppm SO_2 (e.g., Lyons, 2007, 2008). This compares with 10 ppb SO_2 in the modern atmosphere and a few ppm in volcanic plumes. Furthermore, the earlier experiments were carried out under conditions that were appreciably more oxidizing than those appropriate for the Archean atmosphere. We have therefore used the slope of -2.4 for $\Delta^{36}S$-$\Delta^{33}S$ fractionation by SO_2 photodissociation with the self-shielding effect in the 190–220 nm wavelength range and $+0.7$ for photoexcitation in the 240–340 nm range as recommended by Endo et al. (2016).

The equations that characterise the $\Delta^{36}S$-$\Delta^{33}S$ correlation lines have the form $Y = kX + C$, where Y is $\Delta^{36}S$, X is $\Delta^{33}S$, k is the gradient and C is

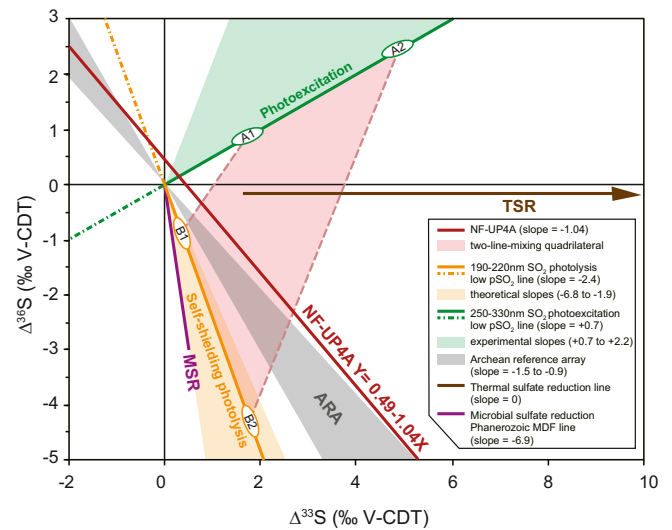**Fig. 3.** A plot of $\Delta^{36}S$ against $\Delta^{33}S$ showing the trend lines for SO_2 photoexcitation (Endo et al., 2016), isotopologue self-shielding photolysis (Endo et al., 2016), microbial sulfate reduction (MSR) (Ono et al., 2006b), and thermochemical sulfate reduction (TSR) (Oduro et al., 2011). The dashed green and yellow lines are the extension of the photochemical experiment lines to negative $\Delta^{33}S$. The green and orange shaded areas show the slope ranges of the photochemical experiment lines under different SO_2 partial pressure (Endo et al., 2016; Masterson et al., 2011; Ono et al., 2013; Whitehill et al., 2013; Whitehill and Ono, 2012). The grey shaded area shows the Archean Reference Array (ARA) (Ono, 2017). Note that the best-fit line for the NF-UP4A data has a positive intercept on the $\Delta^{36}S$ and that none of the experimental fractionation lines have gradients that are close to that of NF-UP4A. The ellipses marked with A_1, A_2, and B_1, B_2, represent end member reservoirs of linear arrays, produced by the two different photochemical reactions. The pale red shaded quadrilateral represents the line-to-line mixing, which cannot produce a linear array. The NF-UP4A trend could be produced by a combination of SO_2 photoexcitation and self-shielding photolysis if the two reactions occurred simultaneously in a single reservoir. (For interpretation of the references to colour in this figure legend, the reader is referred to the web version of this article.)

the intercept on the y ($\Delta^{36}S$) axis. $Y = kX + C$ can be reproduced by combining $Y_1 = k_1X_1$ with $Y_2 = k_2X_2$, if $k_1 > k > k_2$, where (x_1, y_1) is a point on Line 1, and (x_2, y_2) is a point on Line 2. $(x_1 + L_1)$ is the X coordinate of a second point on Line 1 and $(x_2 + L_2)$ is the X coordinate of a second point on Line 2. Since photoexcitation of SO_2 is the only process that yields an array with a gradient > k on a plot of $\Delta^{36}S$ v $\Delta^{33}S$, k_1 must be $+0.7$. The process that yields a gradient < k is photodissociation with self-shielding, so that $k_2 = -2.4$. X and Y for the best-fit lines are given by:

$$X = fX_1 + (1-f) X_2 \tag{1}$$

$$Y = fk_1X_1 + (1-f) k_2X_2 \tag{2}$$

The fraction (f) is defined as the fraction of S from the photoexcitation fractionation line that contributes to the combined line:

$$f = L_2(k - k_2)/\{L_1 (k_1 - k) + L_2 (k - k_2)\} \tag{3}$$

The intercept C is given by.

$$C = (k_1 - k) X_1f - (k - k_2) (1-f) X_2 \tag{4}$$

If $L_2 = L_1$, $f = (k - k_2)/(k_1 - k_2)$, the mixing solution is unique.

Because x_1 and x_2 are linearly correlated with y_1 and y_2, respectively, it can be shown from Eqs. (3) and (4) that when $x_1/L_1 = x_2/L_2$ the combination line ($Y = kX + C$) passes through the origin, whereas if $x_1/L_1 \neq x_2/L_2$, it does not. If $x_1/L_1 > x_2/L_2$ the line has a positive intercept on the y-axis but a negative intercept if $x_1/L_1 < x_2/L_2$. If $x_1/L_1 > x_2/L_2$ the positive intercept increases as $(x_1/L_1)/(x_2/L_2)$ increases and if x_1/L_1
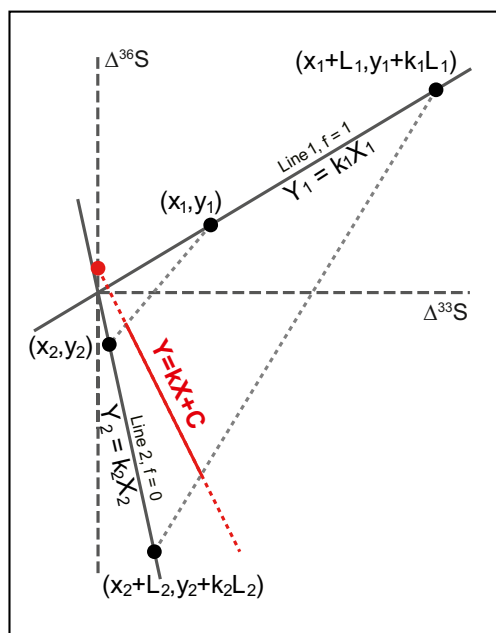
Fig. 4. Diagram used to illustrate the model described in the text to produce the observed $\Delta^{36}S$ vs. $\Delta^{33}S$ fractionation lines by combining SO_2 photoexcitation with SO_2 self-shielding photolysis. Line 1 represents SO_2 photoexcitation and Line 2 SO_2 self-shielding photolysis. The line to be modelled is $Y = kX + C$.

$< x_2/L_2$ the negative intercept increases with decreasing $(x_1/L_1)/(x_2/L_2)$.

There is a continuum of solutions if $L_2 \neq L_1$. This continuum has been modelled using python (see *Supplementary materials*), assuming a single value of f for combining the possible end members. As noted above k_2 (photodissociation with self-shielding) has been set at -2.4 and the range of $\Delta^{33}S$ (in per mil) used is 0 to 22, which is consistent with the experimentally observed range of $\Delta^{33}S$ reported by Endo et al. (2016). The $\Delta^{36}S/\Delta^{33}S$ for photoexcitation (k_1) is assumed to be 0.7. Values for f have been calculated for three ranges of $\Delta^{33}S$ (in per mil), based on experimentally observed ranges, to evaluate their influence on f: Model 1, 0–142 (Ono, 2017); Model 2, 13–142 (Endo et al., 2016; Whitehill and Ono, 2012; Whitehill et al., 2013); and Model 3, 118–142 (Endo et al., 2016). In all three models, x_1 was varied from the start of the range to the end in increments of 0.2, and the length ranges of $\Delta^{33}S$ for L_1 and L_2 were varied from the maximum value as follows: Model 1, L_1 in increment of -4 and L_2 in increment of -0.4; Model 2, L_1 in increment of -2 and L_2 in increment of -0.2; and in Model 3, both L_1 and L_2 were varied in increment of -0.2. As a consequence, all possible combinations of x_1, L_1, and L_2 were canvassed within the stated limits. The solution frequency of f for NF-UP4A is shown in Fig. 5. Note that the mode and medium values for f are about 0.09 in Models 1 and 2 but reduce to 0.06 for Model 3. Halving the X_2 range to 0–11, while maintaining the range of X_1, halves f whereas halving the range of X_1 while maintaining X_2 doubles the value of f. Extending the range of $\Delta^{33}S$ to negative values (-4) in Model 1, for example, has little influence on the calculated values for f (see Model 4, Fig. 5).

The mean, mode, median, minimum, and maximum solutions for f are listed in Table 2. Values for the median and mean, take NF-UP4A for example, are similar: with the mean > median for Models 1, 2, and 4 but the mean slightly less than the median for Model 3 (Table 2, Fig. 5). It is worth noting that the solutions for the modelled combined fractionation line could have variable $\Delta^{33}S$ magnitudes and ranges, and as expected, some exceed those observed in the Archean sedimentary suites (Table A.1) due to high $\Delta^{33}S$ magnitudes and wide $\Delta^{33}S$ ranges from the photochemical experiments. During transfer and deposition of atmospheric sulfur, MIF signals can be diluted by mixing of atmospheric

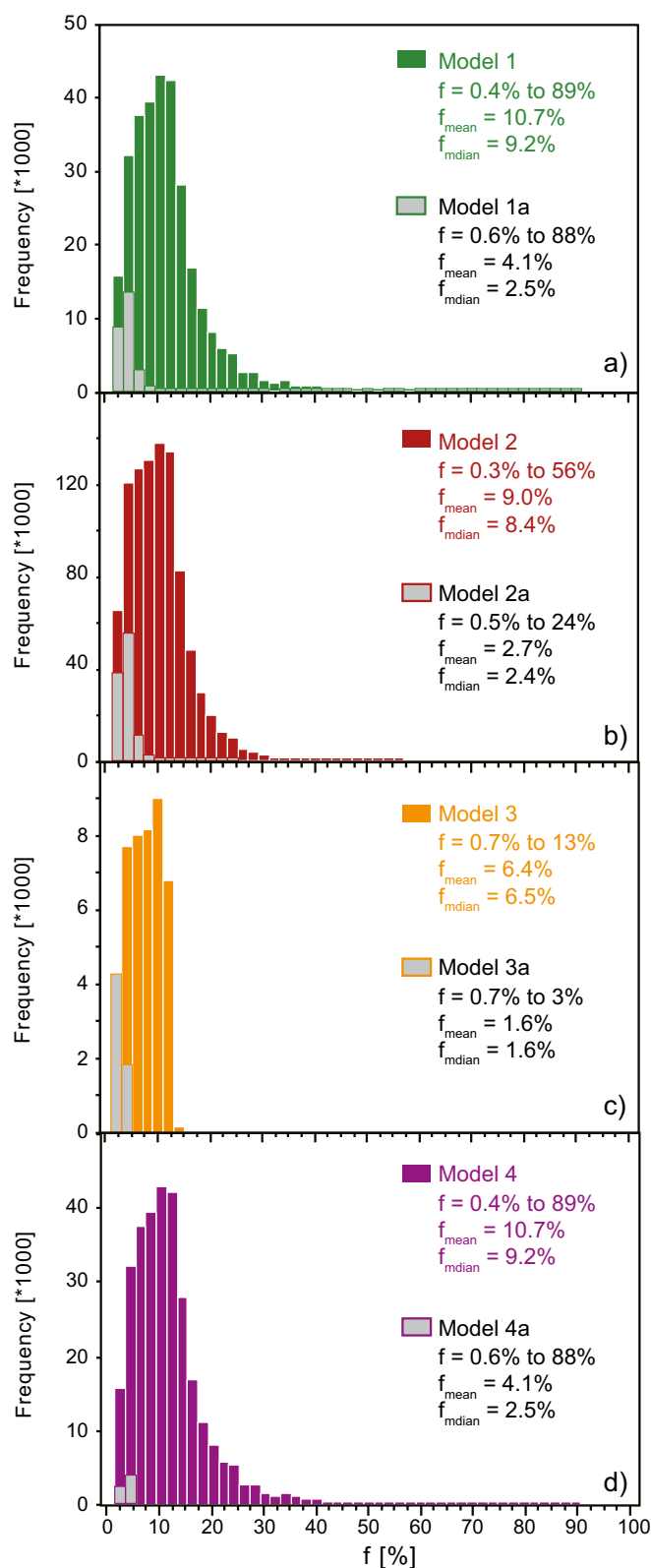**Fig. 5.** Solution frequency of fraction (f) for NF-UP4A for Models 1–4 (coloured filled bins) and Models 1a-4a (grey filled bins). For Models 1a-4a, the observed $\Delta^{33}S$ magnitudes and ranges of NF-UP4A were taken into account. The fraction (f) is defined as the fraction of S from the SO_2 photoexcitation fractionation line that contributes to the simultaneous fractionation line. See text for detailed description.

Table 2
Statistics of the fraction f for the compiled Archean sedimentary pyrites.

Sample ID	$\Delta36S/\Delta33S$	$\Delta^{36}S$ intercept	Model 1 (0–22 vs 0–142)					Model 2 (0–22 vs 13–142)					Model 3 (0–22 vs 118–142)				
			f_{min}	f_{max}	f_{mean}	f_{median}	f_{mode}	f_{min}	f_{max}	f_{mean}	f_{median}	f_{mode}	f_{min}	f_{max}	f_{mean}	f_{median}	f_{mode}
NGB	−0.853	−0.623	0.003	0.898	0.117	0.103	0.117	0.002	0.582	0.102	0.097	0.117	0.008	0.15	0.077	0.078	0.125
DF1	−1.367	−0.592	0.001	0.821	0.065	0.054	0.062	0.001	0.411	0.055	0.050	0.062	0.004	0.080	0.040	0.040	0.066
DF2	−0.808	−0.205	0.003	0.915	0.125	0.110	0.123	0.002	0.596	0.109	0.103	0.174	0.009	0.157	0.082	0.083	0.131
DF3	no trend																
MNF	−0.467	−0.654	0.005	0.933	0.174	0.161	0.181	0.003	0.699	0.155	0.151	0.181	0.014	0.226	0.12	0.124	0.191
MF_BARITE	−3.558	−0.704															
MF_CHERT	−0.874	0.080	0.003	0.909	0.119	0.105	0.115	0.002	0.577	0.103	0.097	0.163	0.008	0.151	0.077	0.078	0.122
MF_SHALE	−0.635	−0.425	0.004	0.924	0.148	0.134	0.15	0.002	0.649	0.13	0.125	0.209	0.011	0.189	0.099	0.102	0.159
MDG	no trend																
BG	−1.474	−0.030	0.001	0.822	0.059	0.048	0.054	0.001	0.375	0.049	0.045	0.054	0.004	0.072	0.036	0.036	0.058
VF	−1.171	−0.130	0.002	0.872	0.085	0.072	0.116	0.001	0.479	0.072	0.067	0.116	0.005	0.107	0.053	0.054	0.086
MG	no trend																
TGB	−0.737	0.042	0.004	0.92	0.136	0.122	0.134	0.002	0.618	0.119	0.113	0.188	0.01	0.174	0.089	0.091	0.142
TGB_BIF	−1.377	0.351	0.003	0.831	0.071	0.06	0.062	0.002	0.441	0.059	0.054	0.062	0.004	0.082	0.041	0.042	0.066
TGB_CHERT	−0.632	0.022	0.004	0.93	0.151	0.137	0.15	0.002	0.65	0.133	0.127	0.21	0.011	0.194	0.101	0.103	0.159
TGB_VOLC	−0.567	0.029	0.004	0.935	0.161	0.147	0.162	0.002	0.669	0.142	0.137	0.224	0.012	0.208	0.109	0.112	0.171
TGB_SHALE	−0.899	0.342	0.004	0.904	0.12	0.106	0.111	0.003	0.6	0.103	0.096	0.158	0.008	0.146	0.075	0.076	0.118
TF	−1.612	0.232	0.002	0.784	0.051	0.042	0.044	0.001	0.354	0.042	0.038	0.044	0.003	0.059	0.029	0.029	0.047
KCRC	−0.928	0.116	0.003	0.902	0.113	0.099	0.107	0.002	0.558	0.097	0.091	0.153	0.008	0.141	0.072	0.073	0.114
IF	−0.770	−1.074	0.003	0.896	0.126	0.112	0.129	0.002	0.608	0.110	0.105	0.182	0.009	0.156	0.084	0.085	0.137
BF	−0.928	0.200	0.004	0.906	0.115	0.1	0.108	0.002	0.559	0.098	0.092	0.153	0.008	0.141	0.072	0.073	0.114
JF	−0.887	0.888	0.007	0.905	0.129	0.113	0.160	0.005	0.603	0.110	0.103	0.160	0.008	0.147	0.077	0.078	0.119
LF	−1.016	0.281	0.004	0.897	0.105	0.091	0.097	0.002	0.562	0.089	0.083	0.138	0.007	0.127	0.065	0.066	0.103
HF	−0.951	−0.309	0.003	0.896	0.107	0.093	0.105	0.001	0.552	0.093	0.087	0.149	0.007	0.134	0.069	0.070	0.112
CD	no trend																
CF	−1.658	0.264	0.002	0.769	0.048	0.039	0.040	0.001	0.334	0.039	0.035	0.040	0.003	0.054	0.027	0.027	0.043
NF_LOW1	−1.207	0.806	0.005	0.867	0.092	0.079	0.111	0.004	0.5	0.077	0.071	0.111	0.005	0.105	0.052	0.053	0.082
NF_LOW2	−0.977	−0.008	0.002	0.901	0.105	0.091	0.101	0.001	0.542	0.091	0.085	0.145	0.007	0.133	0.067	0.068	0.108
NF_UP1	−0.974	−0.298	0.002	0.895	0.105	0.091	0.146	0.001	0.544	0.09	0.085	0.146	0.007	0.131	0.067	0.068	0.108
NF_UP2	−1.074	−0.654	0.002	0.871	0.093	0.080	0.091	0.001	0.513	0.080	0.074	0.131	0.006	0.117	0.059	0.060	0.097
NF_UP3	−0.897	−0.089	0.003	0.909	0.114	0.100	0.111	0.001	0.568	0.099	0.093	0.158	0.008	0.146	0.074	0.075	0.118
NF_UP4H	−1.579	1.144	0.005	0.783	0.062	0.051	0.046	0.004	0.366	0.052	0.047	0.046	0.004	0.064	0.032	0.033	0.049
NF_UP4A	−1.036	0.492	0.004	0.891	0.107	0.092	0.095	0.003	0.557	0.090	0.084	0.136	0.007	0.125	0.064	0.065	0.101
GF1	−0.855	0.048	0.003	0.908	0.120	0.106	0.116	0.002	0.580	0.104	0.098	0.165	0.008	0.152	0.078	0.079	0.124
GF2	−1.001	−0.414	0.002	0.888	0.101	0.087	0.099	0.001	0.535	0.087	0.081	0.141	0.007	0.127	0.065	0.066	0.105
GF2-STEEP	−1.189	0.319	0.003	0.874	0.088	0.075	0.114	0.002	0.506	0.074	0.068	0.114	0.005	0.104	0.053	0.054	0.084
GF2-SHALLOW	−0.914	−0.994	0.003	0.88	0.108	0.095	0.109	0.001	0.563	0.094	0.089	0.109	0.008	0.133	0.071	0.071	0.116
KNF	−1.007	0.251	0.003	0.896	0.106	0.092	0.140	0.002	0.565	0.090	0.084	0.140	0.007	0.129	0.065	0.067	0.104
MMS1	−0.849	0.173	0.004	0.912	0.124	0.109	0.118	0.002	0.584	0.106	0.1	0.167	0.008	0.154	0.079	0.081	0.125
MMS1_UP	−1.021	0.296	0.004	0.896	0.105	0.092	0.097	0.002	0.562	0.089	0.083	0.138	0.007	0.127	0.065	0.066	0.103
MMS1_LOW	−0.815	0.154	0.004	0.916	0.128	0.113	0.122	0.002	0.594	0.11	0.104	0.173	0.009	0.16	0.082	0.084	0.13
MMS2	−0.845	0.899	0.007	0.909	0.135	0.118	0.167	0.006	0.615	0.115	0.108	0.167	0.008	0.154	0.080	0.082	0.125
MMS2_UP	−1.034	0.716	0.005	0.890	0.110	0.096	0.137	0.004	0.559	0.093	0.087	0.137	0.007	0.126	0.065	0.066	0.102
MMS2_LOW	−0.877	1.386	0.009	0.912	0.136	0.120	0.114	0.008	0.606	0.118	0.110	0.161	0.008	0.153	0.079	0.080	0.121
KIF	−1.582	0.622	0.003	0.792	0.058	0.047	0.046	0.002	0.365	0.047	0.043	0.046	0.003	0.063	0.031	0.032	0.049
KF	−1.260	0.157	0.002	0.858	0.079	0.067	0.104	0.001	0.449	0.066	0.061	0.104	0.005	0.096	0.048	0.048	0.077

sulfur carrying opposite larger MIF anomalies, by S derived from MDF processes. The influence of these processes, though poorly known and difficult to quantify, indicates an unaffected initial atmospheric fractionation line with larger $\Delta^{33}S$ magnitudes and wider $\Delta^{33}S$ ranges. To obtain a minimum estimation of f values for the Archean sedimentary suites, the sulfur contents of the Archean sedimentary pyrites were assumed to consist of purely atmospheric sulfur. A constraint that the f solutions must satisfy the observed $\Delta^{33}S$ distributions was then added. New f solution sets of models 1–4 for NF-UP4A and the Mt. McRae were tested. In the case of NF-UP4A (Models 1a-4a in Fig. 5), the f solutions of models with or without constraint show similar distributions, but total numbers and magnitudes of mean and median solutions for f obtained at the given constraint, decrease significantly by ~7%, from around 11% and 9% to 4% and 2% respectively. Modelling of the Mt. McRae, which has similar $\Delta^{36}S/\Delta^{33}S$ slope to that of NF-UP4A, show a decrease in f values with mean and median values down to 2–3% and 1–2%, consistent with the estimation of Endo et al. (2016). Fig. 6 shows a plot of the mean and medium solutions for f against the $\Delta^{36}S/\Delta^{33}S$ gradient for the data taken from the literature. There is a quadratic polynomial relationship between $\Delta^{36}S/\Delta^{33}S$ and f for the mean and medium for the highest probability solutions (Fig. 6).

As discussed, the process that has been modelled is not an atmospheric mixing (Mishima et al., 2017; Whitehill and Ono, 2012) as might occur, for example, if the S on Line 1 was fractionated at one level in the atmosphere and that on Line 2 at another, and these two reservoirs subsequently mixed. The resulting mixture would not form a straight line but scatter over a broad field between Lines 1 and 2. The model illustrated in Fig. 4 is only viable if the S on Lines 1 and 2 is fractionated simultaneously by two processes in a single reservoir. This is possible because SO_2 has two principal absorption bands within the ultraviolet bandwidth, 240–340 nm and 190–220 nm. As noted earlier, photoexcitation of SO_2 occurs in the former bandwidth, and photodissociation with self-shielding in the later. Since natural sunlight includes both bandwidths, photodissociation with self-shielding and photoexcitation via collision-induced intersystem crossing can occur simultaneously, within the same reservoir, as required by our hypothesis. Our model predicts the relative contributions of photoexcitation and photodissociation required to produce the observed $\Delta^{36}S$-$\Delta^{33}S$ linear arrays and $\Delta^{36}S$ intercepts.

5. Potential factors controlling the Archean $\Delta^{36}S/\Delta^{33}S$ distribution

Changes in $\Delta^{36}S/\Delta^{33}S$ with time have been attributed to variations in atmospheric chemistry, including: (i) changes in CH_4 (organic haze; Domagal-Goldman et al., 2008; Izon et al., 2015; Zerkle et al., 2012), (ii) fluctuation in oxygen (Ohmoto et al., 2006; Ono et al., 2006a), (iii) changes in SO_2/H_2S (Halevy et al., 2010), and (iv) increased self-shielding effect due to enhanced SO_2 partial pressure (Ono et al., 2013). Our study shows that variations in f control changes in $\Delta^{36}S/\Delta^{33}S$ but changes in f could, in turn, be controlled by changes in atmospheric chemistry. It is also worth noting that f values might change with altitude as self-shielding photolysis is expected to be dependent on the altitude (Ono et al., 2003). The problem is too poorly constrained to provide a definitive answer but enhanced SO_2 partial pressure is the most likely candidate because it controls photodissociation with self-shielding and therefore influences f. The plot of $\Delta^{36}S/\Delta^{33}S$ against time shows no evidence of a systematic relationship between these variables (Fig. 7). The observed variations in $\Delta^{36}S/\Delta^{33}S$ may be due to global changes in the partial pressure of SO_2 in the atmosphere in response to the waxing and waning of subaerial volcanic activity.

6. Conclusions

The following conclusions can be drawn from this study:

1. The best-fit lines for plots of $\Delta^{36}S$ vs. $\Delta^{33}S$ for many Archean sedimentary pyrite suites do not pass through the origin, requiring the fractionation of $\Delta^{36}S$ and $\Delta^{33}S$ to involve at least two processes.
2. Two processes that can produce the observed Archean $\Delta^{36}S/\Delta^{33}S$ gradients are SO_2 photoexcitation ($\Delta^{36}S/\Delta^{33}S = +0.7$), which occurs in the 240–340 nm bandwidth, and SO_2 photodissociation ($\Delta^{36}S/\Delta^{33}S = -2.4$), which takes place in the 190–220 nm bandwidth.
3. The observed linear relationship between $\Delta^{36}S$ and $\Delta^{33}S$ requires the contribution from the two end-member processes to be in the same proportion over a wide range of $\Delta^{33}S$ values, which precludes mixing between different atmospheric reservoirs of S.
4. However, it can be explained if both photoexcitation via collision-induced intersystem crossing, and photodissociation with self-shielding, occur simultaneously in a single reservoir as is expected when atmospheric SO_2 is exposed to natural light. We suggest this process should be called *simultaneous fractionation*.
5. Numerical modelling shows that variations in $\Delta^{36}S/\Delta^{36}S$ gradients are controlled by changes in f, the fraction of photoexcitation S that contributes to the simultaneous fractionation line. Increasing f increases $\Delta^{36}S/\Delta^{36}S$ gradients.
6. Variations in $\Delta^{36}S/\Delta^{36}S$ gradients are most simply explained by changes in the partial pressure of SO_2 in the atmosphere, which control the relative contributions from photodissociation and photoexcitation to simultaneous fractionation and therefore f.
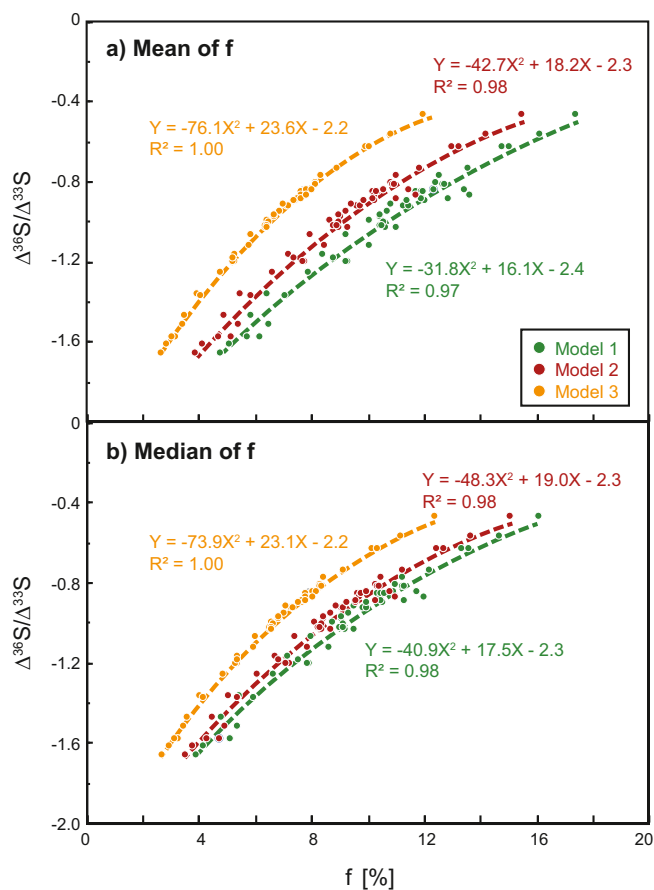

Fig. 6. $\Delta^{36}S/\Delta^{33}S$ plotted against f for the mean (a) and median (b) solutions within three different L ranges for all datasets. The fraction (f) is defined as the fraction of S from the SO_2 photoexcitation fractionation line that contributes to the combined line. There is a quadratic polynomial relationship between $\Delta^{36}S/\Delta^{33}S$ and f for the mean and medium values for all three classes of solution.
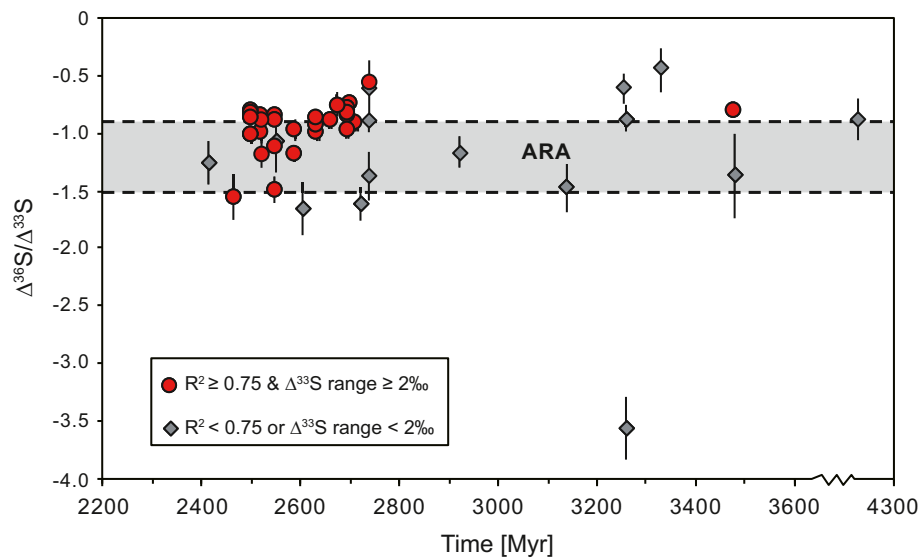
Fig. 7. $\Delta^{36}S/\Delta^{33}S$ plotted against time for the Archean sedimentary pyrites. The grey zone defined by two dashed black lines is the $\Delta^{36}S/\Delta^{33}S$ range of the Archean Reference Array suggested in Ono (2017). Red dots show the gradients for best-fit lines for Archean suites with high reliability ($R^2 \geq 0.75$ and $\Delta^{33}S$ ranges ≥ 2‰), and grey diamonds for those with low reliability ($R^2 < 0.75$ or $\Delta^{33}S$ ranges < 2‰). The error bars are 1-sigma standard deviations for $\Delta^{36}S/\Delta^{33}S$ gradients.

Declaration of Competing Interest

The authors declare that they have no known competing financial interests or personal relationships that could have appeared to influence the work reported in this paper.

Appendix A. Supplementary data

Supplementary data to this article can be found online at https://doi.org/10.1016/j.chemgeo.2021.120640.

References

Busigny, V., Marin-Carbonne, J., Muller, E., Cartigny, P., Rollion-Bard, C., Assayag, N., Philippot, P., 2017. Iron and sulfur isotope constraints on redox conditions associated with the 3.2 Ga barite deposits of the Mapepe Formation (Barberton Greenstone Belt, South Africa). Geochim. Cosmochim. Acta 210, 247–266.

Diekrupa, D., Hanningtona, M.D., Strauss, H., Ginley, S.J., 2018. Decoupling of Neoarchean sulfur sources recorded in Algoma-type banded iron formation. Earth Planet. Sci. Lett. 489, 1–7.

Domagal-Goldman, S.D., Kasting, J.F., Johnston, D.T., Farquhar, J., 2008. Organic haze, glaciations and multiple sulfur isotopes in the Mid-Archean Era. Earth Planet. Sci. Lett. 269, 29–40.

Endo, Y., Danielache, S.O., Ueno, Y., Hattori, S., Johnson, M.S., Yoshida, N., Kjaergaard, H.G., 2015. Photoabsorption cross-section measurements of ^{32}S, ^{33}S, ^{34}S and ^{36}S sulfur dioxide from190 to 220 nm. J. Geophys. Res. Atmos. 120, 2546–2557.

Endo, Y., Ueno, Y., Aoyama, S., Danielache, S.O., 2016. Sulfur isotope fractionation by broadband UV radiation to optically thin SO$_2$ under reducing atmosphere. Earth Planet. Sci. Lett. 453, 9–22.

Farquhar, J., Bao, H., Thiemens, M., 2000. Atmospheric Influence of Earth's Earliest Sulfur Cycle. Science 289, 756–758.

Farquhar, J., Savarino, J., Airieau, S., Thiemens, M.H., 2001. Observation of wavelength-sensitive mass-independent sulfur isotope effects during SO$_2$ photolysis: Implications for the early atmosphere. J. Geophys. Res. Planets 106, 32829–32839.

Farquhar, J., Johnston, D.T., Wing, B.A., Habicht, K.S., Canfield, D.E., Airieau, S., Thiemens, M.H., 2003. Multiple Sulphur isotopic interpretations of biosynthetic pathways: implications for biological signatures in the Sulphur isotope record. Geobiology 1, 27–36.

Farquhar, J., Peters, M., Johnston, D.T., Strauss, H., Masterson, A., Wiechert, U., Kaufman, A.J., 2007. Isotopic evidence for Mesoarchaean anoxia and changing atmospheric Sulphur chemistry. Nature 449, 706–709.

Farquhar, J., Cliff, J., Zerkle, A.L., Kamyshny, A., Poulton, S.W., Claire, M., Adams, D., Harms, B., 2013. Pathways for Neoarchean pyrite formation constrained by mass-independent sulfur isotopes. Proc. Natl. Acad. Sci. U. S. A. 110, 17638–17643.

Galić, A., Mason, P.R.D., Mogollón, J.M., Wolthers, M., Vroon, P.Z., Whitehouse, M.J., 2017. Pyrite in a sulfate-poor Paleoarchean basin was derived predominantly from elemental sulfur: evidence from 3.2 Ga sediments in the Barberton Greenstone Belt, Kaapvaal Craton. Chem. Geol. 449, 135–146.

Gallagher, M., Whitehouse, M.J., Kamber, B.S., 2017. The Neoarchaean surficial Sulphur cycle: an alternative hypothesis based on analogies with 20th-century atmospheric lead. Geobiology 15, 385–400.

Halevy, I., Johnston, D.T., Schrag, D.P., 2010. Explaining the Structure of the Archean Mass-Independent Sulfur Isotope Record. Science 329, 204.

Izon, G., Zerkle, A.L., Zhelezinskaia, I., Farquhar, J., Newton, R.J., Poulton, S.W., Eigenbrode, J.L., Claire, M.W., 2015. Multiple oscillations in Neoarchaean atmospheric chemistry. Earth Planet. Sci. Lett. 431, 264–273.

Izon, G., Zerkle, A.L., Williford, K.H., Farquhar, J., Poulton, S.W., Claire, M.W., 2017. Biological regulation of atmospheric chemistry en route to planetary oxygenation. Proc. Natl. Acad. Sci. U. S. A. 114, E2571–E2579.

Johnson, J.E., Webb, S.M., Thomas, K., Ono, S., Kirschvink, J.L., Fischer, W.W., 2013. Manganese-oxidizing photosynthesis before the rise of cyanobacteria. Proc. Natl. Acad. Sci. U. S. A. 110, 11238–11243.

Johnston, D.T., Farquhar, J., Canfield, D.E., 2007. Sulfur isotope insights into microbial sulfate reduction: when microbes meet models. Geochim. Cosmochim. Acta 71, 3929–3947.

Kaufman, A.J., Johnston, D.T., Farquhar, J., Masterson, A.L., Lyons, T.W., Bates, S., Anbar, A.D., Arnold, G.L., Garvin, J., Buick, R., 2007. Late Archean biospheric oxygenation and atmospheric evolution. Science 317, 1900–1903.

Kurzweil, F., Claire, M., Thomazo, C., Peters, M., Hannington, M., Strauss, H., 2013. Atmospheric sulfur rearrangement 2.7 billion years ago: evidence for oxygenic photosynthesis. Earth Planet. Sci. Lett. 366, 17–26.

Labidi, J., Cartigny, P., Hamelin, C., Moreira, M., Dosso, L., 2014. Sulfur isotope budget (^{32}S, ^{33}S, ^{34}S and ^{36}S) in Pacific-Antarctic ridge basalts: a record of mantle source heterogeneity and hydrothermal sulfide assimilation. Geochim. Cosmochim. Acta 133, 47–67.

Lyons, J.R., 2007. Mass-independent fractionation of sulfur isotopes by isotope-selective photodissociation of SO$_2$. Geophys. Res. Lett. 34, 1–5.

Lyons, J.R., 2008. Photolysis of long-lived predissociative molecules as a source of mass-independent isotope fractionation: the example of SO$_2$. Adv. Quantum Chem. 55, 57–74.

Masterson, A.L., Farquhar, J., Wing, B.A., 2011. Sulfur mass-independent fractionation patterns in the broadband UV photolysis of sulfur dioxide: pressure and third body effects. Earth Planet. Sci. Lett. 306, 253–260.

Mishima, K., Yamazaki, R., Satish-Kumar, M., Ueno, Y., Hokada, T., Toyoshima, T., 2017. Multiple sulfur isotope geochemistry of Dharwar Supergroup, Southern India: late Archean record of changing atmospheric chemistry. Earth Planet. Sci. Lett. 464, 69–83.

Montinaro A, Strauss, H., Mason, P. R. D., Roerdink, D., Münker, C., Schwarz-Schampera, U., Arndt, N. T., Farquhar, J., Beukes, N. J., Gutzmer, J. and Peters, M. (2015) Paleoarchean sulfur cycling: Multiple sulfur isotope constraints from the Barberton Greenstone Belt, South Africa. Precambrian Res. 267, 311–322.

Muller, E., Philippot, P., Rollion-Bard, C., Cartigny, P., Assayag, N., Marin-Carbonne, J., Mohan, M.R., Sarma, S., 2017. Primary sulfur isotope signatures preserved in high-grade Archean barite deposits of the Sargur Group, Dharwar Craton. India. Precambrian Res. 295, 38–47.

Oduro, H., Harms, B., Sintim, H.O., Kaufman, A.J., Cody, G., Farquhar, J., 2011. Evidence of magnetic isotope effects during thermochemical sulfate reduction. Proc. Natl. Acad. Sci. U. S. A. 108, 17635–17638.

Ohmoto, H., Watanabe, Y., Ikemi, H., Poulson, S.R., Taylor, B.E., 2006. Sulphur isotope evidence for an oxic Archaean atmosphere. Nature 442, 908–911.

Ono, S., 2017. Photochemistry of Sulfur Dioxide and the Origin of Mass-Independent Isotope Fractionation in Earth's Atmosphere. In: Jeanloz, R., Freeman, K.H. (Eds.), Annual Review of Earth and Planetary Sciences, vol. 45. Annual Reviews, Palo Alto, pp. 301–329.

Ono, S., Eigenbrode, J.L., Pavlov, A.A., Kharecha, P., Rumble III, D., Kasting, J.F., Freeman, K.H., 2003. New insights into Archean sulfur cycle from mass-independent sulfur isotope records from the Hamersley Basin, Australia. Earth Planet. Sci. Lett. 213, 15–30.

Ono, S., Beukes, N.J., Rumble, D., Fogel, M.L., 2006a. Early evolution of atmospheric oxygen from multiple-sulfur and carbon isotope records of the 2.9 Ga Mozaan Group of the Pongola Supergroup, Southern Africa. S. Afr. J. Geol. 109, 97–108.

Ono, S., Wing, B., Johnston, D., Farquhar, J., Rumble, D., 2006b. Mass-dependent fractionation of quadruple stable sulfur isotope system as a new tracer of sulfur biogeochemical cycles. Geochim. Cosmochim. Acta 70, 2238–2252.

Ono, S., Beukes, N.J., Rumble, D., 2009. Origin of two distinct multiple-sulfur isotope compositions of pyrite in the 2.5 Ga Klein Naute Formation, Griqualand West Basin, South Africa. Precambrian Res. 169, 48–57.

Ono, S., Whitehill, A.R., Lyons, J.R., 2013. Contribution of isotopologue self-shielding to sulfur mass-independent fractionation during sulfur dioxide photolysis. J. Geophys. Res. Atmos. 118, 2444–2454.

Roerdink, D.L., Mason, P.R.D., Whitehouse, M.J., Reimer, T., 2013. High-resolution quadruple sulfur isotope analyses of 3.2 Ga pyrite from the Barberton Greenstone Belt in South Africa reveal distinct environmental controls on sulfide isotopic arrays. Geochim. Cosmochim. Acta 117, 203–215.

Roerdink, D.L., Mason, P.R.D., Whitehouse, M.J., Brouwer, F.M., 2016. Reworking of atmospheric sulfur in a Paleoarchean hydrothermal system at Londozi, Barberton Greenstone Belt, Swaziland. Precambrian Res. 280, 195–204.

Saitoh, M., Nabhan, S., Thomazo, C., Olivier, N., Moyen, J.F., Ueno, Y., Marin-Carbonne, J., 2020. Multiple Sulfur Isotope Records of the 3.22 Ga Moodies Group, Barberton Greenstone Belt. Geosciences 10, 145.

Shen, Y., Farquhar, J., Masterson, A., Kaufman, A.J., Buick, R., 2009. Evaluating the role of microbial sulfate reduction in the early Archean using quadruple isotope systematics. Earth Planet. Sci. Lett. 279, 383–391.

Thomassot, E., O'Neil, J., Francis, D., Cartigny, P., Wing, B.A., 2015. Atmospheric record in the Hadean Eon from multiple sulfur isotope measurements in Nuvvuagittuq Greenstone Belt (Nunavik, Quebec). Proc. Natl. Acad. Sci. U. S. A. 112, 707–712.

Thomazo, C., Ader, M., Farquhar, J., Philippot, P., 2009. Methanotrophs regulated atmospheric sulfur isotope anomalies during the Mesoarchean (Tumbiana Formation, Western Australia). Earth Planet. Sci. Lett. 279, 65–75.

Thomazo, C., Nisbet, E.G., Grassineau, N.V., Peters, M., Strauss, H., 2013. Multiple sulfur and carbon isotope composition of sediments from the Belingwe Greenstone Belt (Zimbabwe): a biogenic methane regulation on mass independent fractionation of sulfur during the Neoarchean? Geochim. Cosmochim. Acta 121, 120–138.

Turner, J.S., 1973. Buoyancy Effects in Fluids (Cambridge Monographs on Mechanics). Cambridge University Press, Cambridge.

Ueno, Y., Ono, S., Rumble, D., Maruyama, S., 2008. Quadruple sulfur isotope analysis of ca. 3.5 Ga Dresser Formation: New evidence for microbial sulfate reduction in the early Archean. Geochim. Cosmochim. Acta 72, 5675–5691.

Wacey, D., Noffke, N., Cliff, J., Barley, M.E., Farquhar, J., 2015. Micro-scale quadruple sulfur isotope analysis of pyrite from the similar to 3480 Ma Dresser Formation: New insights into sulfur cycling on the early Earth. Precambrian Res. 258, 24–35.

Whitehill, A.R., Ono, S., 2012. Excitation band dependence of sulfur isotope mass-independent fractionation during photochemistry of sulfur dioxide using broadband light sources. Geochim. Cosmochim. Acta 94, 238–253.

Whitehill, A.R., Xie, C., Hu, X., Xie, D., Guo, H., Ono, S., 2013. Vibronic origin of sulfur mass-independent isotope effect in photoexcitation of SO_2 and the implications to the early earth's atmosphere. Proc. Natl. Acad. Sci. U. S. A. 110, 17697–17702.

Whitehill, A.R., Jiang, B., Guo, H., Ono, S., 2015. SO_2 photolysis as a source for sulfur mass-independent isotope signatures in stratospehric aerosols. Atmos. Chem. Phys. 15, 1843–1864.

Williford, K.H., Ushikubo, T., Lepot, K., Kitajima, K., Hallmann, C., Spicuzza, M.J., Kozdon, R., Eigenbrode, J.L., Summons, R.E., Valley, J.W., 2016. Carbon and sulfur isotopic signatures of ancient life and environment at the microbial scale: Neoarchean shales and carbonates. Geobiology 14, 105–128.

Zerkle, A.L., Claire, M.W., Domagal-Goldman, S.D., Farquhar, J., Poulton, S.W., 2012. A bistable organic-rich atmosphere on the Neoarchaean Earth. Nat. Geosci. 5, 359–363.

Zhelezinskaia, I., Kaufman, A.J., Farquhar, J., Cliff, J., 2014. Large sulfur isotope fractionations associated with Neoarchean microbial sulfate reduction. Science 346, 742–744.